Fractal basin boundaries and intermittency in the driven damped pendulum

E. G. Gwinn and R. M. Westervelt
Division of Applied Sciences and Department of Physics, Harvard University, Cambridge, Massachusetts 02138
(Received 16 December 1985)

We numerically study intermittency associated with the coexistence of multiple attractors in the damped, driven pendulum. For some ranges of the control parameters the basins of attraction for attractors with positive and negative average angular velocities are intricately interwoven, and the boundary between basins is a fractal set. We observe intrinsic intermittency due to a crisis, in which two chaotic attractors collide with the fractal boundary that divides their basins of attraction. For control parameters near the crisis, the fractal dimension of the basin boundaries approaches that of the phase space, and a random external forcing torque easily induces extrinsic intermittency. Both noise- and crisis-induced intermittency can produce power spectra $S(\omega) \propto 1/\omega^{\alpha}$, with $\alpha \cong 1$, over several decades in frequency ω.

I. INTRODUCTION

The driven, damped pendulum is a classic nonlinear dynamical system which models many physical phenomena, including radio-frequency–driven Josephson junctions and charge-density-wave transport.[1] Despite the apparent simplicity of its equation of motion, the pendulum displays a rich variety of nonlinear phenomena. The different types of steady states, or attractors, of the driven pendulum and of rf-driven Josephson junctions and the ranges of control parameters for which they occur have been studied extensively in numerical and analog simulations,[1–16] and to a lesser degree in experiments on Josephson junctions.[17–22]

This work focuses on the origins of intermittency and low-frequency noise in the driven, damped pendulum. Intermittency occurs as qualitative changes in the state of a system on time scales much longer than the usual characteristic times. For example, hopping between different dc voltage steps at frequencies orders of magnitude lower than the resonant frequency is experimentally observed in rf-driven Josephson junctions. In devices such as these, intermittency causes poor noise performance, because the long times between hops and the frequency dependence of the power spectra prevent effective averaging.

Two categories of intermittency that have been previously identified and studied in simulations of the driven, damped pendulum are Pomeau-Manneville[8,23] and noise-induced intermittency.[6,24,25] Pomeau-Manneville type-1 intermittency is associated with saddle-node bifurcations, and typically produces a Lorentzian angular velocity power spectrum $S(\omega)=S_0/(\omega^2+\tau^{-2})$, where τ^{-1} is the corner frequency.[26] Pomeau-Manneville type-3 intermittency is generated by trajectories that diverge slowly from an unstable periodic orbit, and can yield a $1/f$ power spectrum.[23,26,27] Noise-induced intermittency is always of concern in experiments on systems with multiple steady states. It occurs when a system is knocked between different attractors by an external stochastic noise source. An example is noise-induced hopping between different dc voltage steps in an rf-driven Josephson junction.

In this paper we investigate the role of multiple basins of attraction and their boundaries in the production of intermittency in the damped, driven pendulum. The extrinsic intermittency induced when external noise forces hopping between attractors is sensitive to the arrangement of the basins of attraction. The basin boundaries are also involved in the production of intrinsic, crisis-induced hopping between metastable basins of attraction when no external noise is present.[24] Both intrinsic and extrinsic intermittency can produce noise with a low-frequency spectrum $S(\omega)$ that scales approximately as $1/\omega$ over several decades in frequency ω. We find intermittency with a $1/\omega$ power spectrum over some ranges of the control parameters for which the basins of attraction are interwoven on arbitrarily small length scales, and the basin boundaries are fractal sets.[24] When present, this complicated geometry causes extraordinary noise sensitivity.

II. NUMERICAL SIMULATIONS

In dimensionless form, the equation of motion for the damped, driven pendulum is

$$d^2\theta/dt^2+(1/Q)d\theta/dt+\sin\theta=\Gamma(t)\ ; \tag{1}$$

$$\Gamma(t)=g\cos\phi+\delta g(t)\ ,$$

$$d\phi/dt=\omega_d\ ,$$

where θ is the angle of elevation of the pendulum, $d\theta/dt$ is the angular velocity, and Q is the quality factor. The driving torque $\Gamma(t)$ is a superposition of a sinusoidal torque with amplitude g, frequency ω_d, and phase $\phi=\omega_d t$, and an optional noise term $\delta g(t)$ which is zero unless stated otherwise. We omit a constant drive torque, which would correspond to dc current bias in a Josephson junction. The torque is normalized so that $\Gamma=1$ is the torque necessary to hold the pendulum stationary at $\theta=\pi/2$, the position of maximum restoring torque, and the dimensionless frequency ω_d is normalized to the pendulum's small-amplitude resonant frequency.

Three control parameters determine the nature of the

pendulum's motion: the sinusoidal drive amplitude g, the drive frequency ω_d, and the quality factor Q. The dynamical variables which constitute the phase space for the three-dimensional system of Eq. (1) are the pendulum angle θ, the angular velocity $d\theta/dt$, and the drive phase ϕ. We denote points in this phase space as $(\theta, d\theta/dt, \phi)$.

A digital minicomputer (either an Apollo DN-460 or a Digital Equipment VAX-11/780) was employed to integrate Eq. (1) using a fourth-order Runge-Kutta algorithm with double-precision arithmetic (15 significant digits) and 300 time steps per drive cycle. Comparison of the analytic and computed solutions for the linearized form of Eq. (1) with zero damping and drive $(1/Q = g = 0)$ gave a numerical precision of nine decimal digits in one cycle. The computer time required for the simulations reported below was substantial, approaching 100 CPU hours in some cases. Unlike electronic analogs, digital computers have the advantage that the external noise level $\delta g(t)$ can be accurately controlled. We found that noise due to slow drifts in electronic analogs induced an unacceptable minimum level of extrinsic low-frequency noise.

III. BASINS OF ATTRACTION AND BASIN BOUNDARIES

Without an external driving force, $\Gamma(t)=0$, Eq. (1) describes the damped motion of a particle in the sinusoidal potential well shown in Fig. 1(a). The particle's possible final states consist of stable equilibria (attractors) at the points $\theta = 2n\pi$, $d\theta/dt = 0$, where n is an integer, and unstable equilibria (saddle points) at the points $\theta = (2n+1)\pi$, $d\theta/dt = 0$. Figure 1(b) shows portions of the basins of attraction for attractors at $(\theta, d\theta/dt) = (2n\pi, 0)$ for $n = -3, -2, \ldots, 2, 3$; alternate basins are shaded. For example, all points in the gray region that crosses the center of Fig. 1(b) flow to the attractor at (0,0). Each basin is bounded by the sets of points $(\theta, d\theta/dt)$ that flow to the saddle points on either side of the attractor as $t \to \infty$; these sets form the stable manifolds of the saddle points and are shown in Fig. 1(b) as the lines which separate different basins of attraction. The direction of the flow on the stable manifolds of the saddle points is indicated in Fig. 1(b) by arrows. The sets of points which flow to the saddle points as $t \to -\infty$ are shown in Fig. 1(b) as lines which spiral out from the saddle points and terminate at the point attractors. These lines form the unstable manifold of the saddles, and the flow along them is towards the attractor.

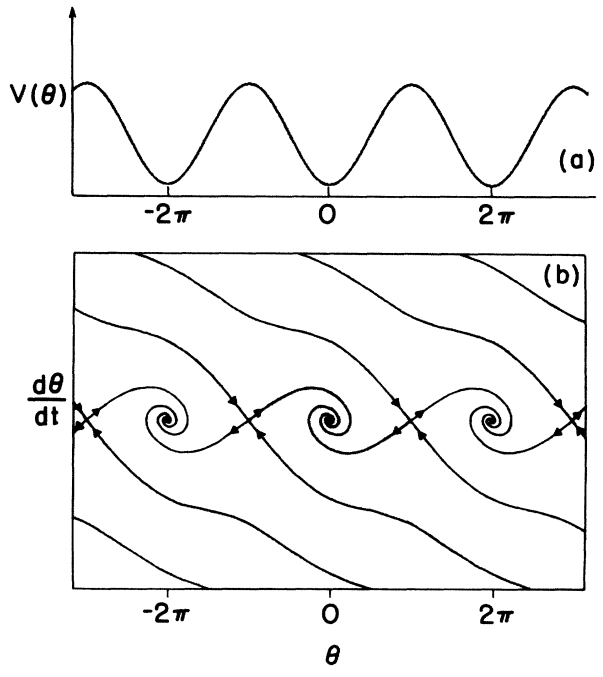

FIG. 1. The damped, undriven pendulum, $Q = 2$. (a) Potential $V(\theta)$. (b) Basins of attraction, attractors, saddle points, and stable and unstable manifolds of saddle points. Attractors are at $(-2\pi, 0)$, (0,0), and $(2\pi, 0)$, and saddle points at $(-3\pi, 0)$, $(-\pi, 0)$, $(\pi, 0)$, and $(3\pi, 0)$. Stable and unstable manifolds of saddle points are shown as heavy lines, with arrows to indicate the direction of the flow. Alternate basins of attraction are shaded.

The addition of a sinusoidal drive torque $\Gamma(t) = g\cos(\omega_d t)$ to Eq. (1) increases the dimension of the phase space from two to three; the new coordinate is the phase $\phi = \omega_d t$ of the drive. Integration of Eq. (1) for one drive cycle defines an invertible map of a plane of constant phase onto itself. Thus, the system's dynamics can be studied on Poincaré sections, which are planes of constant drive phase ϕ (mod 2π). For example, a periodic orbit with the same period as the sinusoidal drive torque appears as a fixed point on a Poincaré section. In all that follows, we compute Poincaré sections at $\phi = 0$, unless stated otherwise; sections at other phases are not qualitatively different.

For small drive amplitudes g such that the magnitude of the angular excursion in θ is much less than π, Poincaré sections of the attractors and their basins are similar to Fig. 1(b). Each of the potential wells of Fig. 1(a) holds a small attracting periodic orbit with period $T = 2\pi/\omega_d$. In Poincaré sections the attractors are single points, and the boundaries that separate their basins are smooth curves.

At larger drive amplitudes g for which the magnitude of the angular excursion in θ approaches or exceeds π, symmetry breaking[1,12] produces pairs of attractors related by the transformation $\theta \to -\theta$, $d\theta/dt \to -d\theta/dt$, $\phi \to \phi + \pi$. These attractors remain distinct when θ is incremented by 2π, unlike the attractors for small g, which can be distinguished only by the number and direction of flips the pendulum makes before reaching the steady state. Symmetry breaking can create pairs of running modes, which are attractors with nonzero average angular velocities: $\langle d\theta/dt \rangle = \pm(m/n)\omega_d$, where m and n are nonzero integers. These attractors correspond to zero-current-bias voltage steps in the resistively shunted Josephson junction, for example.

In the following, we focus on ranges of the control parameters g, Q, and ω_d which produce running modes, and we distinguish between the basin of attraction for all attractors with $\langle d\theta/dt \rangle > 0$ and the basin of attraction for all attractors with $\langle d\theta/dt \rangle < 0$. The boundary that separates these basins can be a fractal set with nonintegral fractal dimension[24] d. The fractal dimension (capacity) of

a set is defined as

$$d = \lim_{\epsilon \to 0} [\ln N(\epsilon)]/[\ln(1/\epsilon)] \quad (2)$$

where $N(\epsilon)$ is the number of cubes of side ϵ required to cover the set.[28,29] On Poincaré sections, basin boundaries with $d > 1$ are fractal; d cannot exceed 2 since the sections are two dimensional.

In nonlinear oscillators such as the pendulum, fractal basin boundaries are typically formed by horseshoes, as discussed by MacDonald *et al.*[30] A horseshoe is an invertible map that compresses, stretches, and folds a rectangle into a strip with one or more horseshoe-shaped bends, as illustrated schematically in Figs. 2(a)–2(c). Under the map, which corresponds to integration of a rectangle of initial conditions on a Poincaré section for an integral number of drive cycles, the rectangle R in Fig. 2(a) is compressed and stretched into an S-shaped strip, as illustrated in Fig. 2(b). The first image of the rectangle R is shown in Fig. 2(c) as the S-shaped area. The fixed points $P1$ and $P2$ shown in Figs. 2(a)–2(c) are saddle points of the map. The bends in the rectangle's image in Fig. 2(c) are mapped outside the original domain; thus, the region R does not contain attractors.

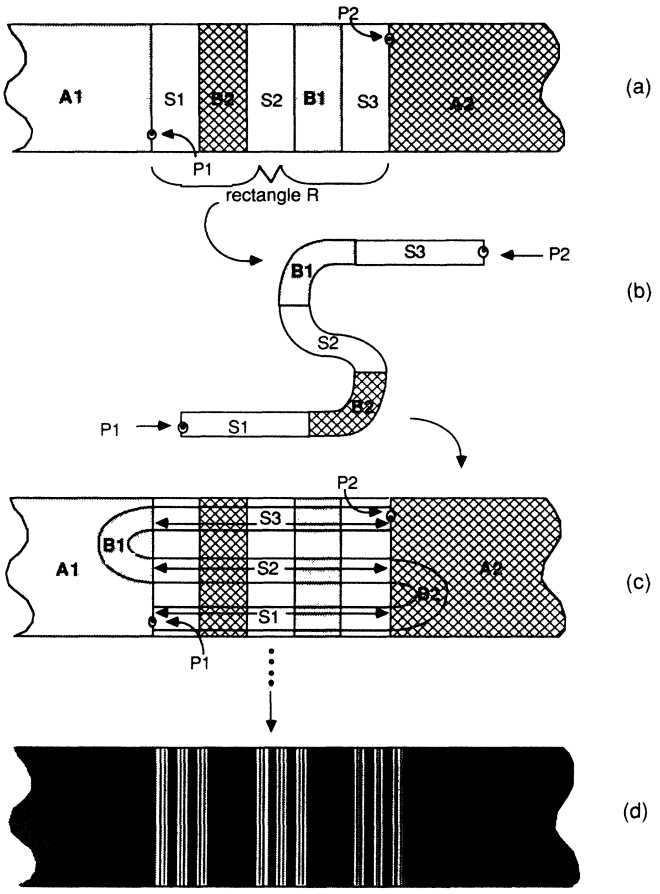

FIG. 2. Formation of a fractal basin boundary by a horseshoe map. The nature of the map in regions $A1$ and $A2$ is unspecified; the map is such that it forms an attractor in each of these areas. (a) The initial rectangle R is bounded by the saddle points $P1$ and $P2$. (b) Intermediate stage of the transformation of R into an S-shaped strip. (c) The S-shaped area is the first image of R under the map. (d) Basin structure determined by applying the map to R three times. The basin of attraction for the attractor in $A1$ shown as gray, the basin of attraction for the attractor in $A2$ as black, and the fate of the white regions is not yet determined.

The details of the map outside the rectangle R, which is bounded by the saddle points $P1$ and $P2$, determine the location and nature of attractors. These may be fixed points, limit cycles, or chaotic attractors. If, in Fig. 2(a), the form of the map in the rectangular regions $A1$ and $A2$ is such that each holds an attractor, the action of the horseshoe map on R creates two basins of attraction that are divided by a fractal boundary. This can be illustrated by dividing R into the vertical strips $S1$, $S2$, $S3$, $B1$, and $B2$, as shown in Fig. 2(a). On one iteration of the map, $B1$ is mapped into the basin of attraction for the attractor in $A1$, and $B2$ into the basin of attraction for the attractor in $A2$; $S1$, $S2$, and $S3$ are mapped to horizontal strips, as indicated in Fig. 2(c). Segments of each of the areas $S1$, $S2$, and $S3$ now overlap the original positions of $B1$ and $B2$. On the next iteration of the map, the parts of $S1$, $S2$, and $S3$ which lie in the cross-hatched region will be sent into $A1$, and the segments that lie in the gray area into $A2$. If these regions were indicated in Fig. 2(a), they would appear as two narrow vertical strips, compromising a portion of each basin, in each of the areas $S1$, $S2$, and $S3$. Thus, each iteration of the horseshoe map determines the attractor to which a set of increasingly narrow vertical strips will go. The basin structure determined by applying the map to the rectangle R three times is shown in Fig. 2(d). The gray regions are mapped to the attractor in $A1$, the black regions are mapped to the attractor in $A2$, and the white regions are still undetermined. The stable manifolds of the two saddle points $P1$ and $P2$ form the boundary of the basins of attraction. Ultimately, all of the rectangle R, excluding a subset of measure zero, the basin boundary, is mapped to the attractor in $A1$ or to the attractor in $A2$. A cut across the basins of attraction intersects the basin boundary in a Cantor set. The dimension of the basin boundary is $1+d$, the sum of the dimension 1 in the linear direction and the dimension d of the fractal cross section. For a more detailed description of the horseshoe map described above, see McDonald *et al.*[30] Guckenheimer and Holmes[31] provide a thorough mathematical treatment of horseshoes. Grebogi *et al.*[32,33] and McDonald *et al.*[30,34] give several examples of maps that exhibit fractal basin boundaries.

Figures 3(a)–3(c) show the basins of attraction for running modes in the driven, damped pendulum at drive phase $\phi = 0$ for $Q = 2$, $\omega_d = \frac{2}{3}$, and three drive amplitudes: $g = 1.46$, 1.48, and 1.4954. The basin of attraction for $\langle d\theta/dt \rangle > 0$ is shown as black, and the basin of attraction for $\langle d\theta/dt \rangle < 0$ as white. The basins are plotted from $\theta = -2\pi$ to 2π to emphasize their periodic structure, and Poincaré sections of the attractors are plotted from $\theta = -\pi$ to π. A small white region has been introduced around the attractors in order to make them visible.

The basins of attraction are computed for a 128×128 grid of initial conditions $(\theta, d\theta/dt, 0)$ spanning $0 \le \theta \le 2\pi$ and $-3.15 \le d\theta/dt \le 3.15$. For each initial condition, we discard an initial transient of at least 30 drive cycles; in

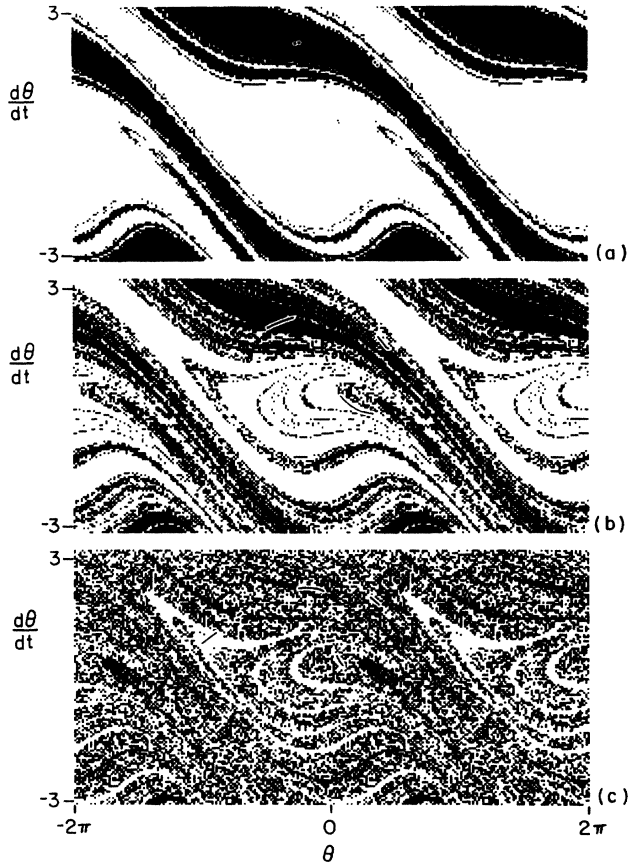

FIG. 3. Basins of attraction for $Q=2$, $\omega_d=\frac{2}{3}$. Basins for attractors with positive average angular velocity are shown as black, and for negative average angular velocity as white. Attractors are plotted from $-\pi$ to π. (a) $g=1.46$. Attractors are periodic. Calculated dimension of basin boundary is 1.63. (b) $g=1.48$. Attractors are chaotic. Calculated dimension of basin boundary is 1.88. (c) $g=1.4954$. Attractors are chaotic. Calculated dimension of basin boundary is 1.97.

some cases, transients exceeding 100 cycles are required for convergence to an attractor. The average velocity over the following ten cycles was used to determine the assignment of the initial condition to the corresponding basin of attraction. Histograms of the average velocity computed in this way displayed well-defined pairs of positive and negative peaks, indicating that this procedure is valid.

In Fig. 3(a), computed for $g=1.46$, the attractors are a pair of period-4 running modes. Two points from the period-4 attractor with $\langle d\theta/dt\rangle=+\omega_d$ lie at $\theta\cong-\pi/4$, $d\theta/dt\cong2.2$, and the other two points at $\theta\cong\pi/3$, $d\theta/dt\cong1.7$. For the period-4 attractor with $\langle d\theta/dt\rangle=-\omega_d$ two points lie at $\theta\cong0$, $d\theta/dt\cong1.1$ (not resolved), and two points at $\theta\cong\pi/10$, $d\theta/dt\simeq0.2$. The large-scale structure of the basins of attraction for these periodic attractors resembles the undriven case illustrated in Fig. 1(b), but on small scales the basins of Fig. 3(a) are mixed in narrow zones that separate the large, solid regions.

Figures 3(b) and 3(c) show the basins of attraction for pairs of chaotic attractors. In Fig. 3(b), for $g=1.48$, the two bands of each of the attractors fall in approximately the same positions as the pairs of points from the periodic attractors described above, and have the same average angular velocities. In Fig. 3(c), for $g=1.4954$, three bands of the chaotic attractor with $\langle d\theta/dt\rangle=+\frac{2}{3}\omega_d$ lie at $\theta\cong-3\pi/4$, $d\theta/dt\cong1.5$; at $\theta\cong-\pi/5$, $d\theta/dt\cong2.2$; and at $\theta\cong2\pi/5$, $d\theta/dt\cong1.8$. The three bands of the chaotic attractor with $\langle d\theta/dt\rangle=-\frac{2}{3}\omega_d$ appear at $\theta\cong-\pi$, $d\theta/dt\cong1.0$; at $\theta\cong0$, $d\theta/dt\cong1.1$; and at $\theta\cong\pi/10$, $d\theta/dt\cong0.3$. Although the largest width of the basins decreases, and the degree of mixing increases from Fig. 3(a) to Fig. 3(c), the structure of the basins is similar in all three cases. For each drive amplitude, the basin boundary is a fractal set formed by the stable manifolds of a pair of saddle orbits with the same average angular velocity as the attractors; the folded structure of the boundaries in Fig. 3 is typical of nonlinear oscillators. Cuts taken perpendicular to the approximately diagonal basins of attraction intersect the basin boundary in a Cantor set, as in the horseshoe map described above. In the full three-dimensional phase space the boundaries of the basins of attraction have the form of highly folded sheets that are smooth in the direction corresponding to the drive phase ϕ. In the direction normal to the sheets, they are spaced in a Cantor-set structure, as illustrated in Fig. 3.

We compute the fractal dimension of the basin boundaries shown in Fig. 3 by a method developed by Grassberger and Procaccia.[35] They show that a lower bound for the fractal dimension of an attractor can be obtained from the integral $C(r)$ of the standard correlation function:

$$C(r)\equiv\lim_{N\to\infty}\left[(1/N^2)\sum_{i,j=1}^{N}\Theta(r-|x_i-x_j|)\right], \qquad (3)$$

where Θ is the Heaviside function, and the points x_i are drawn from a time series on the attractor. For small r, $C(r)$ scales as r^{ν}. The exponent ν characterizes the distribution of probability on the attractor. When the distribution is constant, $\nu=d$, where d is the fractal dimension defined in Eq. (2). In general, the distribution of probability on attractors is not constant and therefore[35] $\nu\leq d$. Because we locate the basins of attraction by direct search, we have $\nu=d$ for the fractal dimension d of the basin boundary. We determine the basin boundary from data such as in Fig. 3 by choosing the x_i to lie halfway between all pairs of nearest neighbors on the grid which go to different attractors. The points x_i thus approximate the basin boundary. We calculate d from the least-squares fit to $C(r)=\alpha r^d$, where α is a constant. The computed fractal dimensions of the basin boundaries shown in Figs. 3(a)–3(c) are, respectively, $d=1.64$, 1.88, and 1.97. For spatially random white noise, $d=2$. Even when the attractor is simple and periodic, the basins of attraction can be highly interwoven and the basin boundary can be a fractal set, as shown in Fig. 3(a). As discussed below, this fact can result in extraordinary sensitivity to added external noise.

As discussed by Grebogi *et al.*,[32] in systems with fractal basin boundaries the predictability of final states given uncertain initial conditions can increase very slowly as the

uncertainty in the initial conditions is reduced. If the initial conditions are specified with error ϵ, the fate of all points within ϵ of the basin boundary is uncertain. The fractal $f(\epsilon)$ of initial conditions in a D-dimensional phase space for which the final state cannot be predicted with certainty scales with ϵ as[32]

$$f(\epsilon) \propto \epsilon^{D-d} . \tag{4}$$

When d approaches D, a large reduction in ϵ produces little improvement in predictive power. For $d=1.64$, as in Fig. 3(a), a factor of 7 reduction in ϵ reduces f by a factor of 2, and for $d=1.97$, as in Fig. 3(c), decreasing ϵ by 10 orders of magnitude only improves the predictability of final states by a factor of 2.

Equation (4) provides an independent measure of the fractal dimension d of the basin boundary which is very useful when d is close to the dimension D of the space in which it is embedded. To estimate $f(\epsilon)$ for the driven pendulum, we compute the final state for 500 randomly chosen initial conditions $(\theta, d\theta/dt, 0)$ and for the surrounding points $(\theta-\epsilon, d\theta/dt, 0)$, $(\theta+\epsilon, d\theta/dt, 0)$, $(\theta, d\theta/dt-\epsilon, 0)$, and $(\theta, d\theta/dt+\epsilon, 0)$ with $\epsilon=10^{-5}$, 10^{-4}, 10^{-3}, and 10^{-2}. If any one of the four surrounding points does not converge to the same attractor as the center point $(\theta, d\theta/dt, 0)$, this point is counted as uncertain and contributes to $f(\epsilon)$. The dimensions estimated in this way for $g=1.46$, 1.48, and 1.4954 are, respectively, 1.61, 1.90, and 1.93, in reasonable agreement with the results above.

Fractal basin boundaries are common in the regions of parameter space that support running modes. For drive amplitudes ranging from $g=1.3$ to 1.5 at fixed quality factor $Q=2$ and drive frequency $\omega_d=\frac{2}{3}$, the boundary dividing the basins of attraction for attractors with $\langle d\theta/dt\rangle=\pm(m/n)\omega_d$ is a fractal set in all of the cases we have tested. To characterize this region of parameter space we computed Figs. 4(a) and 4(b), which are phase diagrams that indicate the steady-state behavior of the pendulum for $Q=2$, over the range $g=1.4$—1.6, and $\omega_d=0.60$—0.70. The resolution of the figures is $\Delta g=0.02$, $\Delta\omega_d=0.01$ in Fig. 4(a), and $\Delta g=0.002$, $\Delta\omega_d=0.001$ in Fig. 4(b). For each point (g,ω_d) on the grid, the nature of the final state for the initial condition (0,0,0) is indicated. In both Figs. 4(a) and 4(b), white regions indicate periodic attractors with zero average angular velocity $\langle d\theta/dt\rangle=0$; cross-hatching denotes intermittent changes in $\langle d\theta/dt\rangle$; vertical stripes indicate chaotic attractors which are not intermittent, and which have $\langle d\theta/dt\rangle=0$; and horizontal stripes indicate periodic attractors with $\langle d\theta/dt\rangle=\pm\omega_d$. In Fig. 4(a), shading denotes periodic final states with $\langle d\theta/dt\rangle=\pm\frac{1}{2}\omega_d$, and diagonal stripes indicate chaotic attractors with $\langle d\theta/dt\rangle=\pm\omega_d$. The black regions in Fig. 4(b) indicate periodic attractors with $\langle d\theta/dt\rangle=\pm\frac{2}{3}\omega_d$, and in the gray regions, the final state for (0,0,0) is a chaotic attractor with $\langle d\theta/dt\rangle=\pm\frac{2}{3}\omega_d$.

In Figs. 4(a) and 4(b), all gray shaded, black, and horizontally striped regions are hysteretic, because they contain pairs of symmetry-related running modes, and the final state is determined by the initial condition. In these regions, the basins of attraction for running modes with $\langle d\theta/dt\rangle=(m/n)\omega_d$ and for $\langle d\theta/dt\rangle=-(m/n)\omega_d$ are divided by a boundary which is fractal in all cases we have investigated. When the dimension d of the basin boundary is a large fraction of the dimension of the phase space, extrinsic intermittency can be induced by small amounts of external noise, as discussed below. Intrinsic intermittency occurs in Figs. 4(a) and 4(b) between zones with different average angular velocities. In both figures, intermittent and phase-locked regions of parameter space are interwoven on very small scales in a narrow transition region between large areas that appear to contain only one

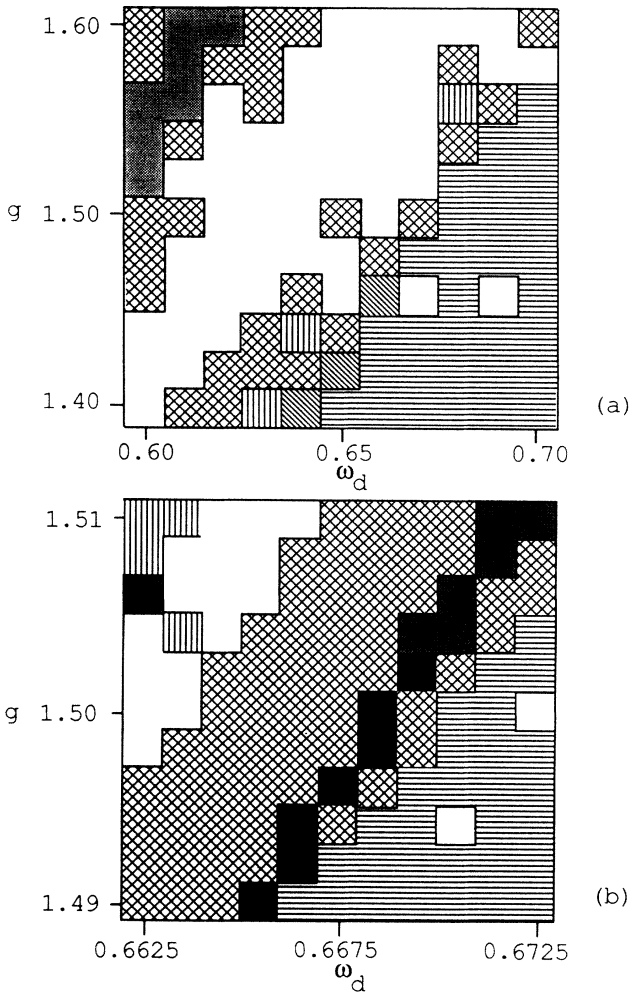

FIG. 4. Phase diagrams centered on $\omega_d=2/3$ and g_c for $Q=2$. In both (a) and (b), the final state of the initial condition (0,0,0) is indicated by cross-hatching for intermittency, vertical stripes for nonintermittent chaos with $\langle d\theta/dt\rangle=0$, white for periodic attractors with $\langle d\theta/dt\rangle=0$, and horizontal stripes for periodic states with $\langle d\theta/dt\rangle=\pm\omega_d$. (a) $0.60<\omega_d<0.70$, $1.40<g<1.60$. Shading denotes periodic attractors with $\langle d\theta/dt\rangle=\pm\frac{1}{2}\omega_d$, and diagonal stripes indicate chaotic attractors with $\langle d\theta/dt\rangle=\pm\omega_d$. (b) $0.6625<\omega_d<0.6725$, $1.49<g<1.51$. Black denotes periodic attractors with $\langle d\theta/dt\rangle=\pm\frac{2}{3}\omega_d$, and gray indicates chaotic attractors with $\langle d\theta/dt\rangle=\pm\frac{2}{3}\omega_d$.

type of behavior. This mixing of regions in parameter space on very small scales to produce phase diagrams with apparently fractal boundaries[11] may reflect the fractal nature of the boundaries of the basins of attraction for fixed parameter values and variable initial conditions.

IV. INTERMITTENCY

We use the term "intermittent" to describe the dynamics of a system that spends long, irregular time intervals in two or more qualitatively different states. A number of different mechanisms produce this behavior.[23,24,26,27,36–43] Nonlinear dynamical systems differ from linear systems in that they can have multiple steady states for the same parameter values. Extrinsic intermittency, which is noise-induced hopping between different attractors, occurs when a system with more than one attractor is coupled to an external stochastic noise source. Intrinsic intermittency occurs in the absence of external noise, and is associated with bifurcations of nonlinear systems as parameter values are varied: Pomeau-Manneville intermittency occurs near the loss of stability of periodic attractors, and crisis-induced intermittency occurs near crises in which chaotic attractors lose stability. In previous work the driven damped pendulum equations have been shown to exhibit Pomeau-Manneville type-1 intermittency,[8,13] crisis-induced intermittency,[24] and noise-induced intermittency.[6,24,25] Figure 5 uses one-dimensional maps to illustrate these types of intrinsic intermittency.

Pomeau-Manneville intermittency results from the loss of stability of a periodic attractor to intermittent chaos through a bifurcation,[36,37] in which the nature of the flow near the bifurcating orbit changes qualitatively as a control parameter is varied. Such bifurcations produce intermittent trajectories that consist of long sequences of nearly periodic behavior, associated with motion near a destabilized attractor, interrupted by chaotic bursts. As illustrated in Fig. 5(a), Pomeau-Manneville type-1 intermittency occurs near a saddle-node bifurcation in which a periodic attractor and an unstable periodic orbit coalesce and annihilate. Long intervals of nearly periodic behavior occur when the trajectory passes through the constricted region near the position of the stable-unstable pair of orbits at the bifurcation. Figure 5(a) shows a segment of a typical trajectory passing through the bottleneck; after it leaves this region it will move chaotically until another portion of the map reinjects it into the constricted zone.

Trajectories that diverge slowly from an unstable periodic orbit generate Pomeau-Manneville type-3 intermittency, which occurs in maps such as the one shown in Fig. 5(b). Trajectories started near the unstable fixed point move away from it slowly if the map is tangent to the diagonal at the fixed point as shown, producing long intervals of nearly periodic behavior. Once out of the neighborhood of the fixed point, trajectories move chaotically until injected close to it again.

Intermittency due to a crisis occurs in systems with multiple attractors. A crisis is the collision of a chaotic attractor with the boundary of its basin of attraction, and can occur in two ways, as discussed by Grebogi *et al.*[44,45] and McDonald *et al.*[34] A boundary crisis destroys the attractor and its basin, resulting in long transients for initial conditions near the destabilized attractor.[44–46] An interior crisis[44,45] merges distinct chaotic attractors into a single attractor on which trajectories move intermittently.[24] This intermittency consists of long intervals of chaotic motion near the precrisis attractors, broken by brief excursions into new regions of the attractor added by the crisis.

Figures 5(c) and 5(d) illustrate intermittency due to a crisis in the logistic map. The unstable fixed point shown in Fig. 5(c) as an open circle and its preimage on the opposite side of the parabolic map bound the basin of attraction for the chaotic attractor shown as a heavy black line. Trajectories started in the interval, delimited by a dotted box, remain in it for all time. At the crisis, the chaotic attractor collides with the unstable fixed point. Figure 5(d) shows the map just beyond the crisis. Trajectories are confined for long times within the dotted box, and leave it only when they fall within a small interval near the maximum of the map. For an interior crisis, orbits which escape the destabilized attractor in this way flow to another, similarly destabilized attractor. The intermittent attractor consists of two or more "metastable attractors" and the paths along which trajectories move between them. The motion consists of long intervals of small-scale chaos near the metastable attractors, interrupted by large-scale chaotic bursts associated with hopping between them.

Extrinsic intermittency occurs in dynamical systems with multiple attractors when external stochastic noise pushes trajectories across basin boundaries, creating noise-induced hopping between attractors. The distribution of lifetimes of the destabilized attractors is determined both by the effect of noise on the attractor, and on

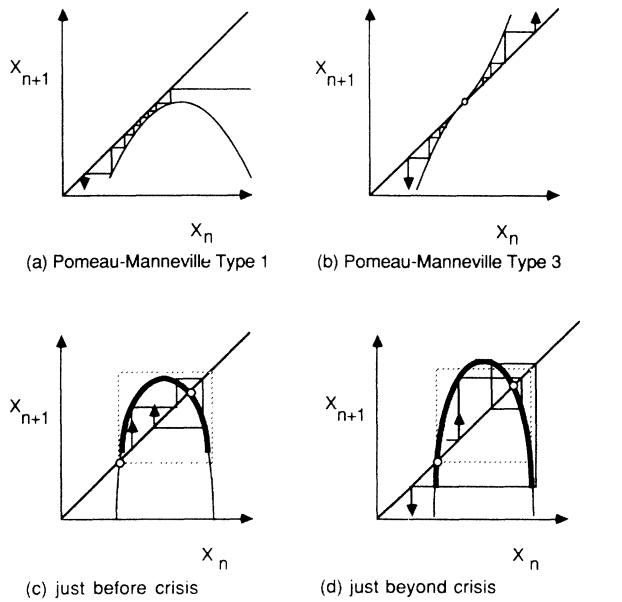

FIG. 5. Illustration of three types of intrinsic intermittency in a 1D quadratic map. Segments of the path of a typical trajectory are indicated by arrows. (a) Pomeau-Manneville type-1 intermittency; (b) Pomeau-Manneville type-3 intermittency; (c) map just before crisis; (d) crisis-induced intermittency.

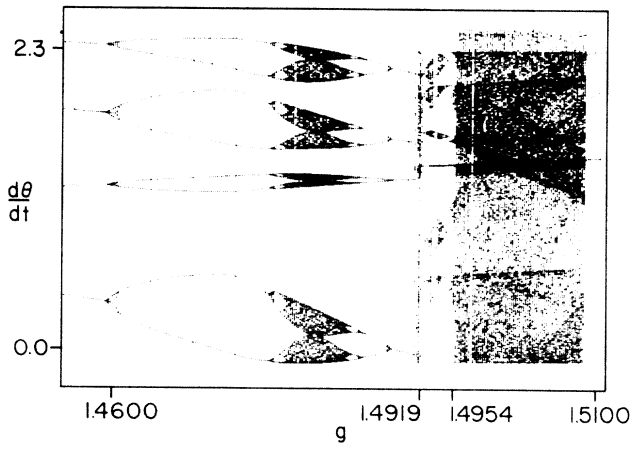

FIG. 6. Bifurcation diagram. The angular velocity is plotted vs g at $\phi=0$ for $\omega_d=\frac{2}{3}$ and $Q=2$.

the geometry of the boundaries of the basins of attraction. As shown below, extrinsic intermittency is enhanced by noise sensitivity of the attractor due to small negative Lyapunov exponents, and by fractal basin boundaries.

An overview of a development of the attractors for the damped, driven pendulum which produces both Pomeau-Manneville type-1 intermittency and crisis-induced intermittency is shown in the bifurcation diagram of Fig. 6. To compute the figure, we locate two initial conditions $(\theta/d\theta/dt,0)$ which converge to the positive and negative running modes for the drive amplitude $g=1.45$, for $Q=2$ and $\omega_d=\frac{2}{3}$. For each initial condition g is increased adiabatically in increments $\Delta g=1\times10^{-4}$ from $g=1.45$ to 1.52. After each increment a transient of 50 drive cycles is allowed for convergence to an attractor. The following 100 values of the angular velocity at drive phase $\phi=0$ are plotted in Fig. 6, and form the bifurcation diagram. When the drive amplitude was decreased from $g=1.52$, a small region just below $g=1.4954$ was found where there are at least four attractors.

For drive amplitudes $1.4500<g<1.4917$ in Fig. 6, the pendulum is phase locked with average angular velocity $\langle d\theta/dt\rangle=\pm\omega_d$. Between $g=1.4917$ and 1.4919 the pendulum is unlocked, and for $1.4920<g<1.4955$ it is locked again with $\langle d\theta/dt\rangle=\pm\frac{2}{3}\omega_d$. From $g=1.51$ to 1.52 all attractors found have zero average angular velocity. Pomeau-Manneville type-1 intermittency occurs near the saddle-node bifurcation at $1.4919<g<1.4920$ which creates a pair of period three attractors with $\langle d\theta/dt\rangle=\pm\frac{2}{3}\omega_d$. These attractors undergo a series of bifurcations which culminates in a period-doubling cascade to chaos. At a critical value $1.4954<g_c<1.4955$, the two chaotic attractors merge through a crisis into a single attractor on which trajectories switch intermittently between states with $\langle d\theta/dt\rangle=\frac{2}{3}\omega_d$ and $-\frac{2}{3}\omega_d$.

The qualitative differences between Pomeau-Manneville type-1, crisis-induced, and extrinsic intermittency are illustrated in Fig. 7, which compares time records of the angular velocity $d\theta/dt$ for a trajectory of each type. Each record is 5000 drive cycles long and is strobed at drive phase $\phi=0$. Figure 7(a) illustrates Pomeau-Manneville type-1 intermittency for g just below the value at which simultaneous saddle-node bifurcations produce a pair of symmetry-related periodic attractors with

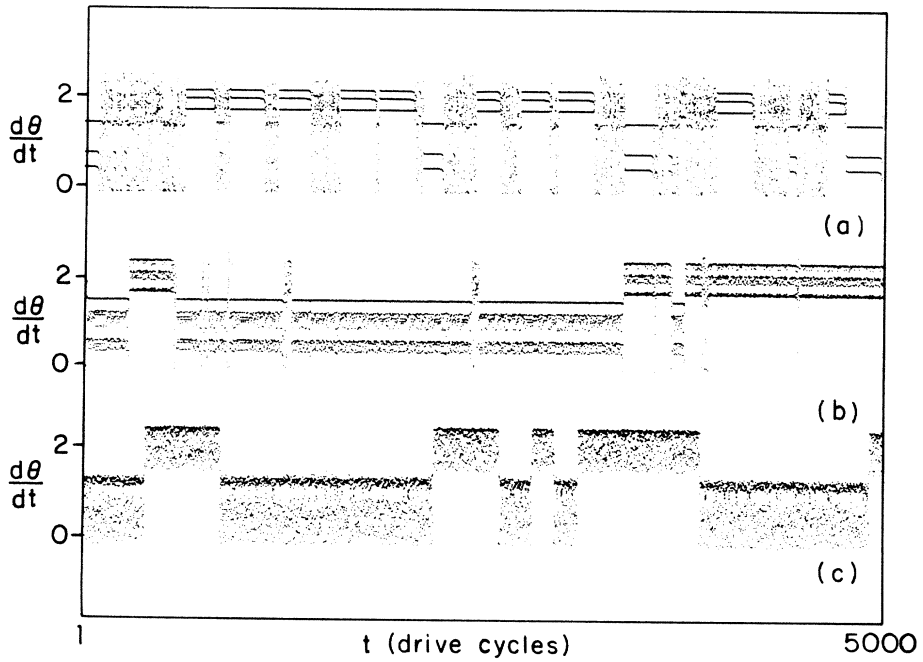

FIG. 7. Intermittent time series of the angular velocity $d\theta/dt$ plotted once per drive cycle at $\phi=0$ for $Q=2$, $\omega_d=\frac{2}{3}$. (a) Pomeau-Manneville type-1 intermittency, $g=1.491\,908$; (b) crisis-induced intermittency, $g=1.495\,46$; (c) extrinsic intermittency, $g=1.46$, $\sigma=0.20$.

$\langle d\theta/dt\rangle = \pm\frac{2}{3}\omega_d$. Long segments of nearly periodic motion occur when the trajectory approaches the location where the periodic attractors appear; these are interrupted by chaotic bursts. Figure 7(b) shows an example of a crisis-induced intermittent trajectory. Here two distinct chaotic attractors with $\langle d\theta/dt\rangle = \pm\frac{2}{3}\omega_d$ have merged via an interior crisis to form a single attractor. Motion on this object consists of long periods of small-scale chaos near the precrisis attractors separated by very brief transitions between them. An example of extrinsic intermittency is shown in Fig. 7(c), which was computed by adding a random noise term $\delta g(t)$ to the drive torque in Eq. (1) for values of the control parameters g, Q, and ω_d which yield a pair of periodic attractors with $\langle d\theta/dt\rangle = \pm\omega_d$ in the absence of noise. As shown, the angular velocity switches irregularly between two noisy bands, which correspond to the two noise-free attractors.

Low-frequency noise is produced by the large changes in amplitude of the angular velocity for the intermittent trajectories in Fig. 7. We use the term low-frequency noise to refer to broadband spectral features in the power spectrum $S(\omega)$ of $d\theta/dt$ at frequencies far below the lowest natural frequency in the linearized version of Eq. (1). The noise power spectra associated with Pomeau-Manneville type-1 and -3 intermittency have been calculated; type 1 typically gives a Lorentzian spectrum,[26] and type 3 produces $1/f$ noise[23,26,27] for certain choices of the shape of the map near the unstable fixed point.

In the pendulum we observe hopping between states with opposite average angular velocities. For crisis-induced intermittency, the states are metastable attractors; for extrinsic intermittency, the states are attractors that have been destabilized by noise. If the lifetimes of the two states and the hopping process are uncorrelated, and the time that trajectories spend moving between states is small, an intermittent variable such as $d\theta/dt$ can be approximated by

$$d\theta/dt = T\,d\theta_1/dt + (1-T)d\theta_2/dt\ , \tag{5}$$

where $T(t)$ is a telegraph signal that switches randomly between 0 and 1, and between 1 and 0, with respective rates $1/\tau_1$ and $1/\tau_2$.[6,47] The angular velocities for the two parts of the trajectory that approach the noise-free or metastable attractors are $d\theta_1/dt$ and $d\theta_2/dt$.

With the assumption that $d\theta_1/dt$, $d\theta_2/dt$, and $T(t)$ are all uncorrelated, the spectrum $S(\omega)$ of $d\theta/dt$ can be shown to be[6,47]

$$S(\omega) = 4(\langle d\theta_1/dt\rangle - \langle d\theta_2/dt\rangle)^2/\{(\tau_1+\tau_2)[\omega^2+(1/\tau_1+1/\tau_2)^2]\} + [\tau_1^2 S_1(\omega)+\tau_2^2 S_2(\omega)]/(\tau_1+\tau_2)^2$$
$$+2[S_1(\omega)+S_2(\omega)] * 1/\{[\omega^2+(1/\tau_1+1/\tau_2)^2](\tau_1+\tau_2)\}\ , \tag{6}$$

where $S_1(\omega)$ and $S_2(\omega)$ are the power spectra for $d\theta_1/dt$ and $d\theta_2/dt$, and the symbol $*$ denotes convolution. Typically, the power spectrum below the fundamental response to the drive frequency of $d\theta_1/dt$ and $d\theta_2/dt$ is dominated by the first term of Eq. (6), which is a Lorentzian with corner frequency $\omega_c = 1/\tau_1 + 1/\tau_2$.

The low-frequency power spectra for uncorrelated hopping between three or more attractors or metastable attractors is the sum of the Lorentzian spectra associated with hopping between pairs of states.[48] This superposition can produce a power-law spectrum $S(\omega) \propto 1/\omega^\alpha$, with $0 \le \alpha \le 2$, over a limited frequency range. When more than three attractors are present, the distribution of characteristic lifetimes determines α. The superposition of a set of Lorentzian spectra with a log-normal distribution of lifetimes produces a good approximation to a $1/\omega$ spectrum over a wide range of frequencies.[49]

V. CRISIS-INDUCED INTERMITTENCY

Figure 8 shows an example of a crisis for the damped, driven pendulum in which a chaotic attractor intersects the basin boundary. Here part of the Poincaré sections computed at zero drive phase $\phi = 0$ is shown for values of the drive amplitude just below, at, and just above the value at which the crisis occurs:[24] $1.4954 < g_c < 1.4955$. The part of the Poincaré section shown is one segment of the three-banded chaotic attractor with $\langle d\theta/dt\rangle = -\frac{2}{3}\omega_d$; two points from a period-6 saddle orbit which lies on the basin boundary are shown as open circles. As g is increased to g_c in Fig. 8, the chaotic attractor approaches the saddle orbit and collides with it at $g = g_c$. A collision between the symmetry-related saddle orbit and attractor with opposite average angular velocity $\langle d\theta/dt\rangle = \frac{2}{3}\omega_d$ occurs simultaneously. Following the crisis, these chaotic attractors merge to form a single un-

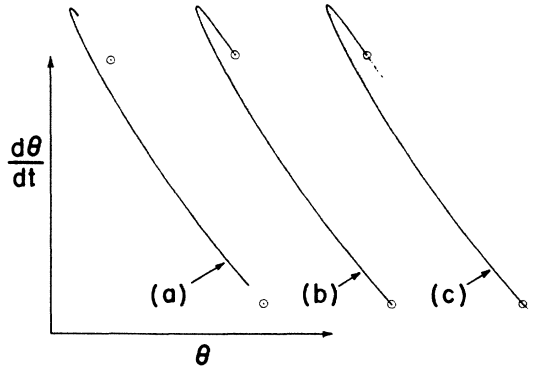

FIG. 8. Development of a crisis. In (a) $g = 1.495\,450$, and in (b) $g = 1.495\,457$. Both (a) and (b) show a detail of a Poincaré section at $\phi = 0$ of the chaotic three-banded attractor with $\langle d\theta/dt\rangle = -\frac{2}{3}\omega_d$, and two points from a period-6 saddle orbit with $\langle d\theta/dt\rangle = -\frac{2}{3}\omega_d$ that lies on the basin boundary. (c) Two points from a period-6 saddle orbit with $\langle d\theta/dt\rangle = -\frac{2}{3}\omega_d$ and the part of the intermittent attractor formed by the crisis that falls within the same phase space area as in (a) and (b), for $g = 1.495\,460$.

locked intermittent attractor, a small piece of which is shown in Fig. 8(c), for $g > g_c$.

A Poincaré section of the entire attractor at $\phi = 0$ is shown in Fig. 9 just beyond the crisis; it is a folded structure which includes the two precrisis attractors. The repetitive folding evident in Fig. 9 is produced by horseshoes in the dynamics on the attractor. Just beyond the crisis, the steady-state trajectories consist of long intervals of chaotic motion near the precrisis attractors, broken by brief excursions through the regions of the attractor which connect these metastable zones. Figure 7(b) illustrates this behavior in a long-time series of the angular velocity strobed at $\phi = 0$.

Histograms of the distribution of angular velocity on the unlocked attractor at $\phi = 0$ are shown in Figs. 10(a)–10(c) for g just below, just above, and well beyond g_c. In Fig. 10(a), just before the crisis, the leftmost three bands in the distribution correspond to the three bands of the chaotic attractor with $\langle d\theta/dt \rangle = -\frac{2}{3}\omega_d$, and the three bands on the right of the figure correspond to the attractor with $\langle d\theta/dt \rangle = \frac{2}{3}\omega_d$. In Fig. 10(b), just beyond the crisis, the velocity distribution near the destabilized attractors is practically unchanged from Fig. 10(a). The crisis has added regions of low probability that connect the bands associated with the separate running modes. Well beyond the crisis, in Fig. 10(c), remnants of the bands corresponding to the positive and negative running modes are still evident, but the structure of the attractor has changed substantially. Previously forbidden ranges of angular velocity are more probable than in Fig. 10(b).

The velocity distribution for all three cases in Fig. 10 is quite complex; it is neither Gaussian nor unimodal, and is apparently not a differentiable curve. The many spikes shown are produced by repetitive folding in the dynamics associated with the presence of horseshoes. Each fold produces a peak in the velocity distribution; a similar effect occurs for the probability distribution of a sine wave. The stretching and folding process is illustrated in Fig. 11, which shows Poincaré sections of the attractor for $g = 1.4955$ as the drive phase increases from $\phi = 0$ in Fig. 11(a) to $\phi = 3\pi/5$ in Fig. 11(d). This folding process is repeated twice each drive cycle; the iterative process of folding and compression as time evolves covers the entire attractor with creases on arbitrarily small size scales.

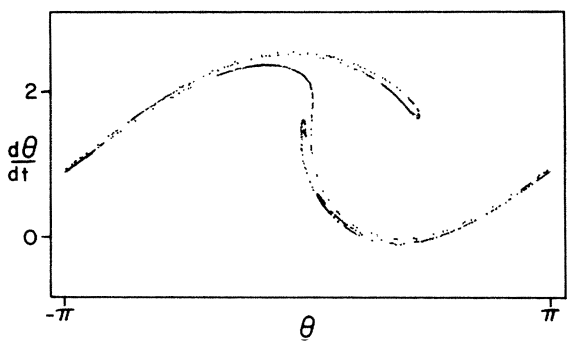

FIG. 9. Intermittent attractor created by a crisis, $g = 1.4955$, $Q = 2$, $\omega_d = \frac{2}{3}$.

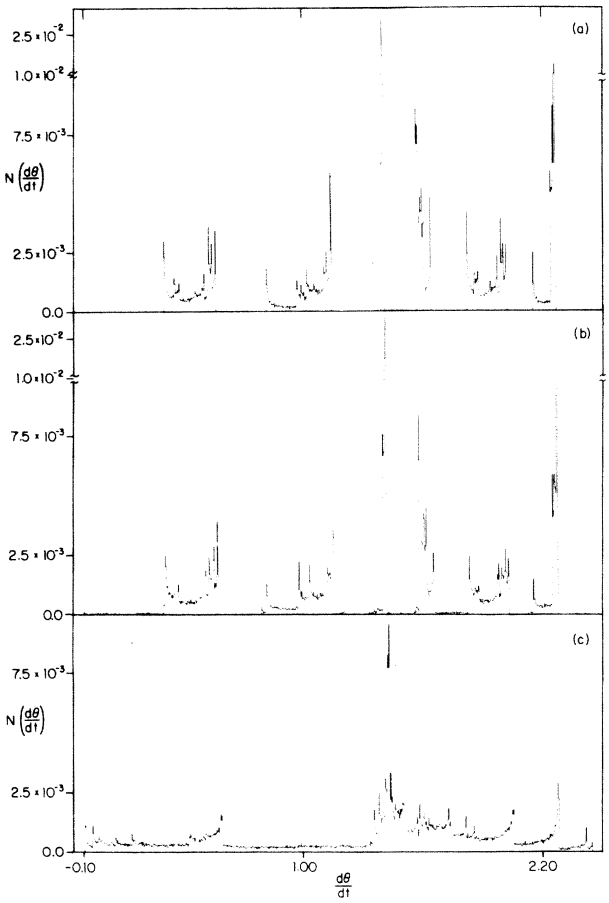

FIG. 10. Histograms of the angular velocity for $Q = 2$, $\omega_d = \frac{2}{3}$. (a) $g = 1.495\,45$; (b) $g = 1.495\,46$; (c) $g = 1.500\,000$.

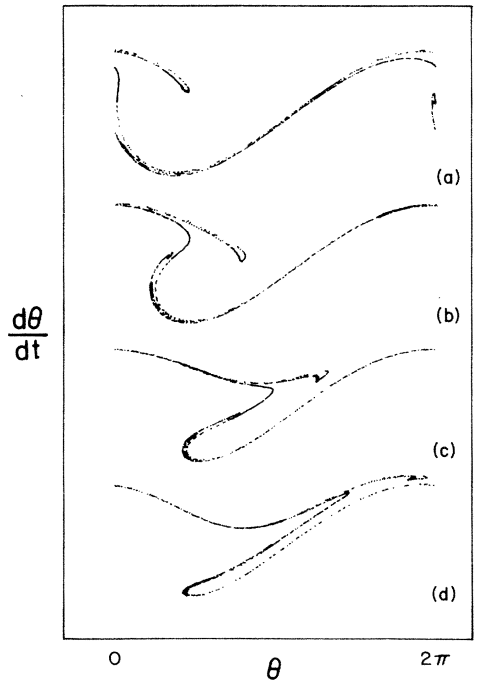

FIG. 11. Development of folds with drive phase ϕ in the intermittent attractor for $g = 1.4955$, $Q = 2$, $\omega_d = \frac{2}{3}$. (a) $\phi = 0$; (b) $\phi = \pi/5$; (c) $\phi = 2\pi/5$; (d) $\phi = 3\pi/10$.

The crisis changes the distribution of probability on the attractor more dramatically than the distribution of the angular velocity. To approximate the probability distribution, we divide the area $0<\theta<2\pi$, $-3<d\theta/dt<3$ on the Poincaré section at $\phi=0$ into a 5000×2500 grid, and count the number of times a trajectory of 200 000 cycles visits each box. For $g<g_c$, below the crisis, trajectories of 100 000 cycles on each of the two chaotic attractors are used. The relative probability, or relative visitation frequency, ρ_i of each box is equal to the fraction of the total number of points in the trajectory that fall within the box: $\rho_i=n_i/n$, where n is the total number of drive cycles. The average recurrence time for box i is $1/\rho_i$ drive cycles. The distribution $N(\rho)$ of the probability is proportional to the number of boxes with probability ρ.

Figure 12 shows histograms of the weighted distribution $\rho N(\rho)$ versus ρ, where the probability ρ and probability distribution $N(\rho)$ are computed as described above, for three values of drive amplitude: Fig. 12(a), g below g_c; Fig. 12(b), g just greater than g_c; and Fig. 12(c), g well above g_c. The weighted distribution $\rho N(\rho)$ is the total probability contained in boxes with relative visitation frequency ρ. If the probability distribution on the attractor were nearly uniform, $N(\rho)$ and $\rho N(\rho)$ would have a single narrow peak at the average value of ρ.

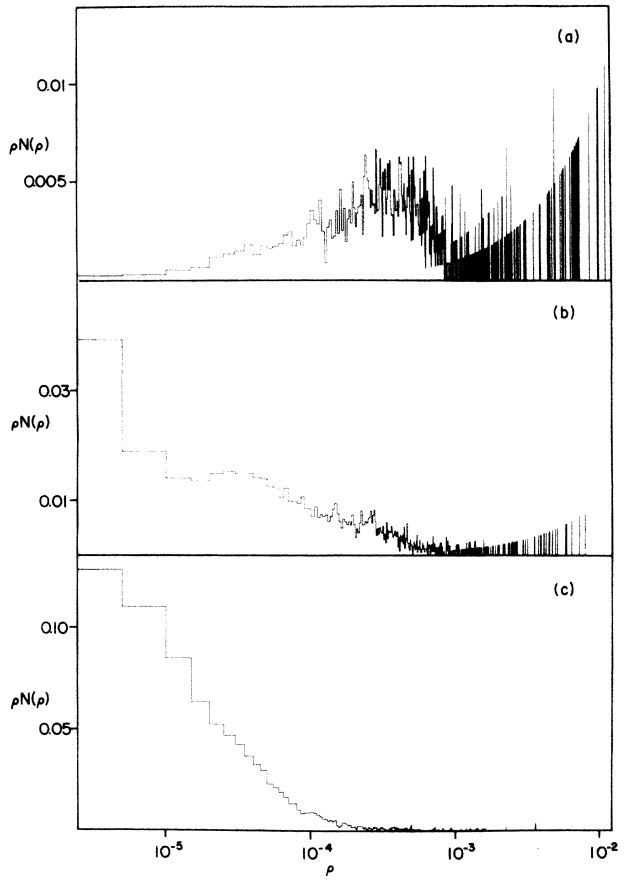

FIG. 12. $\rho N(\rho)$, the total probability contained in boxes with relative probability ρ, is plotted vs ρ for $Q=2$, $\omega_d=\frac{2}{3}$. (a) $g=1.495\,45$; (b) $g=1.495\,46$; (c) $g=1.500\,00$.

As shown in Fig. 12, the actual distribution is much more complex and evolves rapidly as g increases through the crisis. For g just below g_c in Fig. 12(a), the weighted distribution $\rho N(\rho)$ on the two separate chaotic attractors consists of two parts: coherent spikes at high ρ which contain a large fraction of the total probability, and a broad peak at moderate values of ρ which corresponds to diffuse motion connecting the parts of the attractors associated with the spikes. Following the crisis at $g=g_c$ the previously distinct attractors are connected by relatively improbable strands. In Fig. 12(b), for g slightly greater than g_c, this is reflected as an increase in $\rho N(\rho)$ at low ρ, corresponding to long recurrence times, and a decrease in the coherent structure at large ρ. In Fig. 12(c), well beyond the crisis, the coherent spikes at large ρ have nearly disappeared, and the distribution of probability on the attractor is smoother and shifted to low ρ.

The power spectrum $S(\omega)$ of the angular velocity for intrinsic intermittency in the driven damped pendulum is typically Lorentzian, as shown in Fig. 13(b), computed for $g=1.50$. This can be understood empirically (but not precisely) by using the two-state random-hopping model described above, where the two states are the two destabilized running modes and chaotic fluctuations play the role of noise. Just above the crisis, however, the power spectrum $S(\omega)$ has an approximate $1/\omega$ dependence over more than two decades in frequency, as shown in Fig. 13(a). Although trajectories on the attractor switch erratically between well-defined positive and negative running modes, as shown in Fig. 7(b), the two-state random-hopping model given above in Eq. (5), in which the probability per unit time of leaving either state is constant, is apparently inapplicable. Recent work[50] has shown that a narrow $1/\omega$ region appears in the power spectrum for crisis-induced intermittency in the one-dimensional quadratic map. This narrow $1/\omega$ region is attributed to a su-

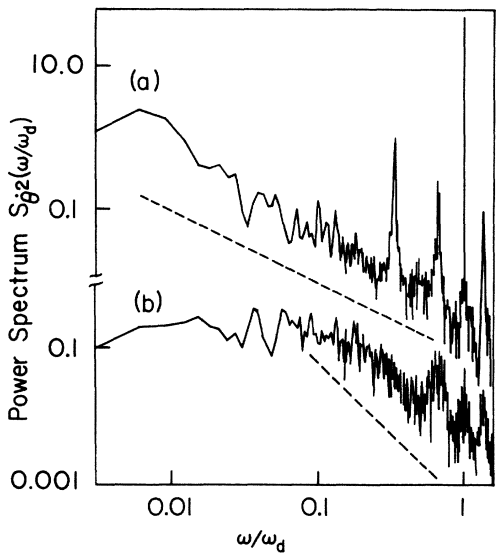

FIG. 13. Angular velocity power spectra of intrinsically intermittent trajectories for $Q=2$, $\omega_d=\frac{2}{3}$. Dashed lines have logarithmic slope -1 and -2. (a) $g=1.4955$; (b) $g=1.5000$.

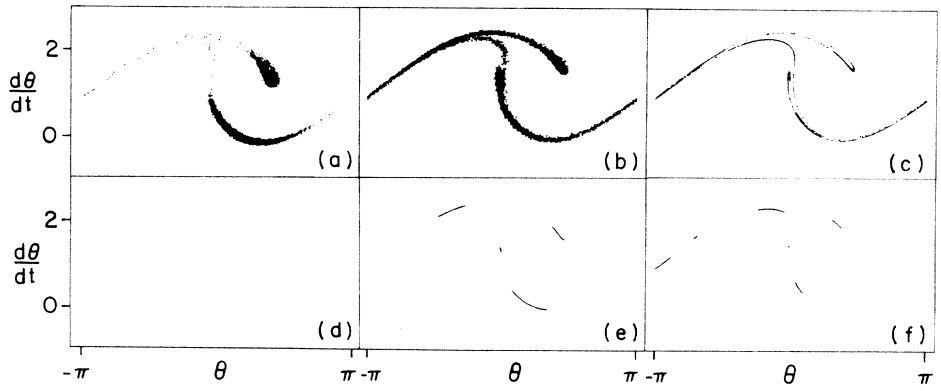

FIG. 14. Extrinsically intermittent attractors created by adding Gaussian noise with standard deviation σ to Eq. (1) for $Q=2$, $\omega_d=\frac{2}{3}$ are shown in (a)–(c); the corresponding noise-free attractors are shown in (d)–(f). (a) $g=1.3000$, $\sigma=0.3500$; (b) $g=1.4800$, $\sigma=0.3500$; (c) $g=1.4954$, $\sigma=0.0100$; (d) $g=1.3000$; (e) $g=1.4800$; (f) $g=1.4954$.

perposition of two Lorentzian spectra and extends over approximately one-half decade in frequency. In Fig. 13, the $1/\omega$ dependence extends over at least two decades in frequency, and cannot be explained by the superposition of only two Lorentzian spectra. Empirically, we find that $1/\omega$ power spectra occur when the path between different metastable attractors is very complex; in this case the power spectrum may be described by the superposition of many Lorentzians.[49] The crisis-induced intermittency discussed here is similar in some respects to noise-induced intermittency discussed below. Metastable "basins of attraction" persist at drive amplitudes just beyond the crisis at g_c. The lifetimes of the destabilized running modes are relatively long, and the computed metastable basins closely resemble Fig. 3(c).

VI. EXTRINSIC INTERMITTENCY

In the absence of external noise, the lifetimes of separate stable running modes of the driven damped pendulum are infinite. In any real physical system, external noise is always present, and will eventually cause transitions between previously stable attractors. As the noise level increases the lifetime of the attractors will decrease. We study the influence of external noise on the driven, damped pendulum by adding a random torque $\delta g(t)$ to the right-hand side of the equation of motion in Eq. (1). Because the amplitude distribution of physical noise sources is usually Gaussian, we add at each integration time step a torque $\delta g(t)$ that is a random number drawn from a normal distribution with standard deviation σ. This noise torque may be regarded as the average of a physical noise source over a time interval equal to the time step $\Delta t=\pi/100$ (300 time steps per drive cycle).

The noise-induced hopping rate and power spectrum are determined both by the effect of noise on the attractors and by the geometry of the basins of attraction. The influence of external noise on the attractor for the running modes described previously is illustrated in Fig. 14, which shows pairs of noise-free and noise-broadened Poincaré sections of the attractor for three different drive amplitudes. In all cases noise broadens the attractor asymmetrically along directions for which compression is weakest, producing an object which strongly resembles the intrinsically chaotic attractor in Fig. 9. Figure 14(d) shows the noise-free attractors at $g=1.30$, and Fig. 14(a) the attractor for the same drive amplitude when Gaussian noise with standard deviation $\sigma=0.35$ is added. The noise-free attractors are periodic with $\langle d\theta/dt\rangle=\pm\omega_d$, as shown in Fig. 14(d). The noise-broadened attractor shown in Fig. 14(a) is elongated along the directions for which the flow toward the attractor is least strongly contracting. Trajectories move erratically between long periods of nearly phase-locked behavior with $\langle d\theta/dt\rangle=\pm\omega_d$. The parts of the attractor in Fig. 14(a) that correspond to this motion are the dark regions at the top for $\langle d\theta/dt\rangle=\omega_d$ and the dark segments at the bottom for $\langle d\theta/dt\rangle=-\omega_d$. Hopping between these modes takes place when the broadened attractor intersects the boundary of the basin of attraction, along the thin filaments that connect the dark regions.

The influence of external noise on chaotic attractors is illustrated in Figs. 14(b) and 14(c), which show Poincaré sections of the chaotic running modes for $g=1.48$ and 1.4954, respectively, which were discussed above. As shown, external noise tends to spread the attractors along the directions in which the flow is expanding, producing an object which strongly resembles the unlocked intermittent attractor. The basins of attraction for $g=1.48$ are shown in Fig. 3(b); the basin boundaries are highly folded with fractal dimension $d=1.88$. The noise-free chaotic attractors for this drive amplitude shown in Fig. 14(e) approach the basin boundary more closely than the periodic attractors in Fig. 14(d), and hopping between attractors is more easily induced by external noise. In Fig. 14(f), for $g=1.4954$, just below the crisis at g_c, the dimension of the basin boundary is close to 2, and the separation between the attractors and the basin boundaries is extremely small. In this case intermittency is induced by a very small noise level and produces the attractor shown in Fig. 14(c) for $\sigma=0.01$. This noise-broadened attractor is practically identical to the intrinsically intermittent attractor shown in Fig. 9.

Far from the crisis, the attractors and the basin boundary are separated by a finite distance, and the dimension

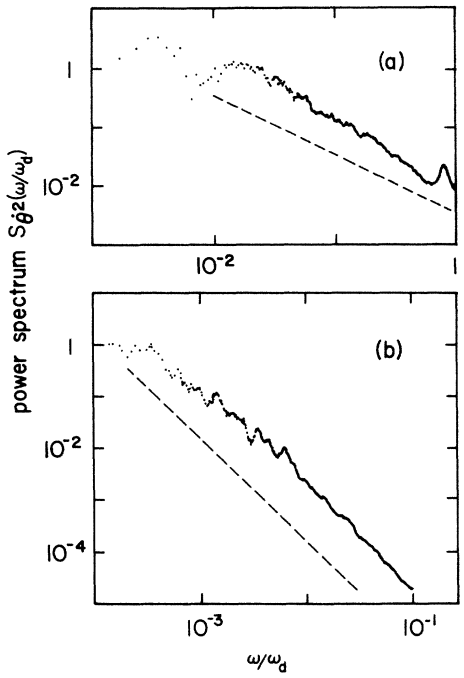

FIG. 15. Angular velocity power spectra of extrinsically intermittent trajectories for $Q=2$, $\omega_d=\frac{2}{3}$. Dashed lines have logarithmic slope of -1 and -2. (a) $g=1.4954$, $\sigma=0.0100$; (b) $g=1.4600$, $\sigma=0.2000$.

of the basin boundary is substantially less than 2. The noise level required to produce extrinsic intermittency on accessible time scales is large enough to smear histograms of the angle θ and the angular velocity $d\theta/dt$ into distributions with smooth peaks near each of the noise-free attractors. In this situation, it is reasonable to adopt the model for random hopping between two states described above. The observed angular velocity power spectra far from the crisis are Lorentzian, with a corner frequency that decreases with the noise level σ. Figure 15(b) shows a representative spectrum computed for $g=1.46$ and $\sigma=0.20$. However, near the crisis the small noise level required to induce intermittency produces probability distributions similar to the intrinsic case which yields $1/\omega$ noise. Just below the crisis, noise-induced intermittency also produces an approximate $1/\omega$ spectrum $S(\omega)$ as shown in Fig. 15(a), computed for $g=1.4954$ and $\sigma=0.01$. The mechanisms that produce this frequency dependence are unclear, but are empirically associated with the highly divided geometry of the basins of attraction near the crisis, as discussed above.

VII. CONCLUSIONS

The driven, damped pendulum is a classic example of a driven nonlinear oscillator, and its behavior is representative of a large class of systems. We have studied the influence of crises and of fractal boundaries of the basins of attraction on both intrinsic and noise-induced intermittency in the driven, damped pendulum. Fractal basin boundaries with large fractal dimension produce extraordinary sensitivity to external noise, and interior crises induce intrinsic intermittency. Extrinsic and crisis-induced intermittency can be difficult to distinguish from power spectra alone. For both cases, the velocity power spectra are typically Lorentzian, but are found to be $1/\omega$ when the fractal dimension of the basin boundary approaches the dimension of the phase space, and near an interior crisis. The actual behavior observed in experiments on pendula and rf-driven Josephson junctions will be determined by the values of the operating parameters and the extrinsic noise level.

ACKNOWLEDGMENTS

We thank M. Beasley, C. Grebogi, E. Ott, J. A. Yorke, B. B. Mandelbrot, S. W. Teitsworth, M. Iansiti, and M. Tinkham for helpful discussions. This work was supported in part by the U.S. Office of Naval Research under Contract No. N00014-84-K-0329. One of us (E.G.G.) acknowledges support from AT&T Bell Laboratories.

[1]A. H. Macdonald and M. Plischke, Phys. Rev. B **27**, 201 (1983).
[2]E. Ben-Jacob and D. J. Bergman, Phys. Rev. A **29**, 2021 (1984).
[3]B. A. Huberman, J. P. Crutchfield, and N. H. Packard, Appl. Phys. Lett. **37**, 750 (1980).
[4]R. L. Kautz, J. Appl. Phys. **52**, 3528 (1981).
[5]R. L. Kautz, J. Appl. Phys. **52**, 6241 (1981).
[6]R. L. Kautz, J. Appl. Phys. **58**, 424 (1985).
[7]N. F. Pederson and A. Davidson, Appl. Phys. Lett. **39**, 830 (1981).
[8]W. J. Yeh and Y. H. Kao, Appl. Phys. Lett. **42**, 299 (1983).
[9]M. Octavio, Phys. Rev. B **29**, 1231 (1984).
[10]I. Goldhirsch, Y. Imry, G. Wasserman, and E. Ben-Jacob, Phys. Rev. B **29**, 1218 (1984).
[11]E. G. Gwinn and R. M. Westervelt, in *Proceedings of the 17th International Conference on Low Temperature Physics, Karlsruhe, West Germany, 1984,* edited by U. Eckern, A. Schmid, W. Weber, and H. Wuhl (North-Holland, Amsterdam, 1984), p. 1139.
[12]D. D'Humieres, M. R. Beasley, B. A. Huberman, and A. Libchaber, Phys. Rev. A **26**, 3483 (1982).
[13]H. Seifert, Phys. Lett. **98A**, 213 (1983).
[14]P. Alstrom and M. T. Levinsen, Phys. Rev. B **31**, 2753 (1985).
[15]Da-Ren He, W. J. Yeh, and Y. H. Kao, Phys. Rev. B **31**, 1359 (1985).
[16]H. Koga, H. Fujisaka, and M. Inoue, Phys. Rev. A **28**, 2370 (1983).
[17]R. F. Miracky, J. Clarke, and R. H. Koch, Phys. Rev. Lett. **50**, 856 (1983).
[18]V. N. Gubankov, K. I. Konstantinyan, V. P. Koshelets, and

G. A. Ovsyannikov, IEEE Trans. Magn. **MAG-19**, 637 (1983).
[19]M. Octavio and C. Readi Nasser, Phys. Rev. B **30**, 1586 (1984).
[20]Q. Hu, J. U. Free, M. Iansiti, O. Liengme, and M. Tinkham, IEEE Trans. Magn. **MAG-21**, 590 (1985).
[21]C. Vanneste *et al.*, Phys. Rev. B **31**, 4230 (1985).
[22]P. C. Cronemeyer, C. C. Chi, A. Davison, and N. F. Pederson, Phys. Rev. B **31**, 2667 (1985).
[23]R. F. Miracky, M. H. Devoret, and J. Clarke, Phys. Rev. A **31**, 2509 (1985).
[24]E. G. Gwinn and R. M. Westervelt, Phys. Rev. Lett. **54**, 1613 (1985).
[25]M. Iansiti, Qing Hu, R. M. Westervelt, and M. Tinkham, Phys. Rev. Lett. **55**, 746 (1985).
[26]A. Ben-Mizrachi, I. Procaccia, N. Rosenberg, and A. Schmidt, Phys. Rev. A **31**, 1830 (1985).
[27]I. Proccacia and H. Schuster, Phys. Rev. A **28**, 1210 (1983).
[28]B. B. Mandelbrot, *The Fractal Geometry of Nature* (Freeman, San Francisco, 1983).
[29]J. Farmer, E. Ott, and J. A. Yorke, Physica **7D**, 153 (1983).
[30]S. W. McDonald, C. Grebogi, E. Ott, and J. A. Yorke, Physica **17D**, 125 (1985).
[31]J. Guckenheimer and P. Holmes, *Nonlinear Oscillations, Dynamical Systems, and Bifurcations of Vector Fields* (Springer-Verlag, New York, 1983).
[32]C. Grebogi, S. W. McDonald, E. Ott, and J. A. Yorke, Phys. Lett. **99A**, 415 (1983).
[33]C. Grebogi, E. Ott, and J. A. Yorke, Phys. Rev. Lett. **50**, 935 (1983).
[34]S. W. McDonald, C. Grebogi, E. Ott, and J. A. Yorke, Phys. Lett. **107A**, 51 (1985).
[35]P. Grassberger and I. Proccacia, Phys. Rev. Lett. **50**, 346 (1983).
[36]Y. Pomeau and P. Manneville, Commun. Math. Phys. **74**, 189 (1980).
[37]P. Manneville, J. Phys. (Paris) **41**, 1235 (1980).
[38]G. Mayer-Kress and H. Haken, Physica (Utrecht) **10**, 329 (1984).
[39]F. T. Arecchi, R. Badii, and A. Politi, Phys. Rev. A **29**, 1006 (1984).
[40]T. Geisel and S. Thomae, Phys. Rev. Lett. **52**, 1936 (1984).
[41]T. Geisel, J. Nierwetberg, and A. Zacherl, Phys. Rev. Lett. **54**, 616 (1985).
[42]J. P. Eckmann, Rev. Mod. Phys. **53**, 643 (1981).
[43]J. E. Hirsch, B. A. Huberman, and D. J. Scalapino, Phys. Rev. A **25**, 519 (1982).
[44]C. Grebogi, E. Ott, and J. A. Yorke, Physica (Utrecht) **7D**, 181 (1983).
[45]C. Grebogi, E. Ott, and J. A. Yorke, Phys. Rev. Lett. **48**, 1507 (1982).
[46]F. T. Arecchi, R. Badii, and A. Politi, Phys. Lett. **103A**, 3 (1984).
[47]M. R. Beasley, D. D'Humieres, and B. A. Huberman, Phys. Rev. Lett. **50**, 1328 (1983).
[48]F. T. Arecchi, R. Badii, and A. Politi, Phys. Rev. A **32**, 402 (1985).
[49]E. W. Montroll and M. F. Shlesinger, Proc. Natl. Acad. Sci. (USA) **79**, 3380 (1982).
[50]Y. Yamaguchi and H. Minowa, Phys. Rev. A **32**, 3758 (1985).

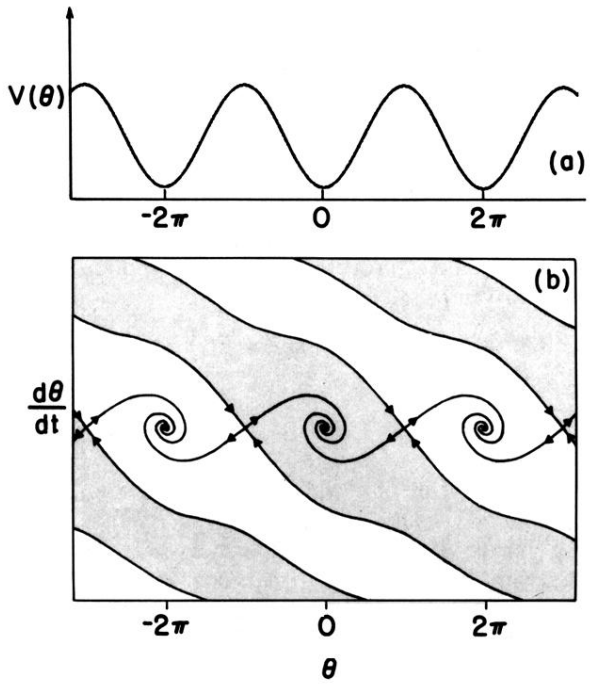

FIG. 1. The damped, undriven pendulum, $Q=2$. (a) Potential $V(\theta)$. (b) Basins of attraction, attractors, saddle points, and stable and unstable manifolds of saddle points. Attractors are at $(-2\pi,0)$, (0,0), and $(2\pi,0)$, and saddle points at $(-3\pi,0)$, $(-\pi,0)$, $(\pi,0)$, and $(3\pi,0)$. Stable and unstable manifolds of saddle points are shown as heavy lines, with arrows to indicate the direction of the flow. Alternate basins of attraction are shaded.

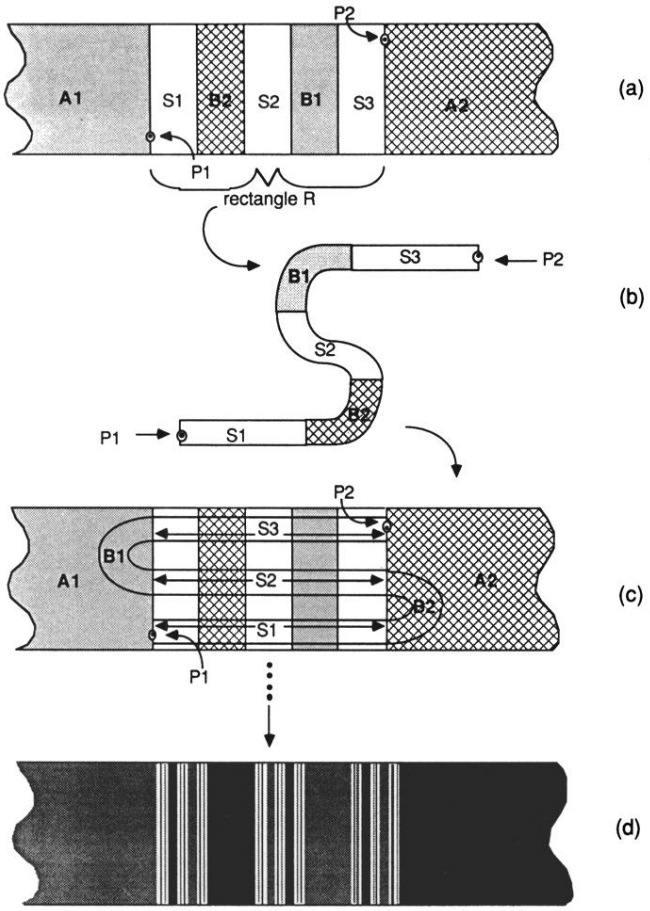

FIG. 2. Formation of a fractal basin boundary by a horseshoe map. The nature of the map in regions $A1$ and $A2$ is unspecified; the map is such that it forms an attractor in each of these areas. (a) The initial rectangle R is bounded by the saddle points $P1$ and $P2$. (b) Intermediate stage of the transformation of R into an S-shaped strip. (c) The S-shaped area is the first image of R under the map. (d) Basin structure determined by applying the map to R three times. The basin of attraction for the attractor in $A1$ shown as gray, the basin of attraction for the attractor in $A2$ as black, and the fate of the white regions is not yet determined.

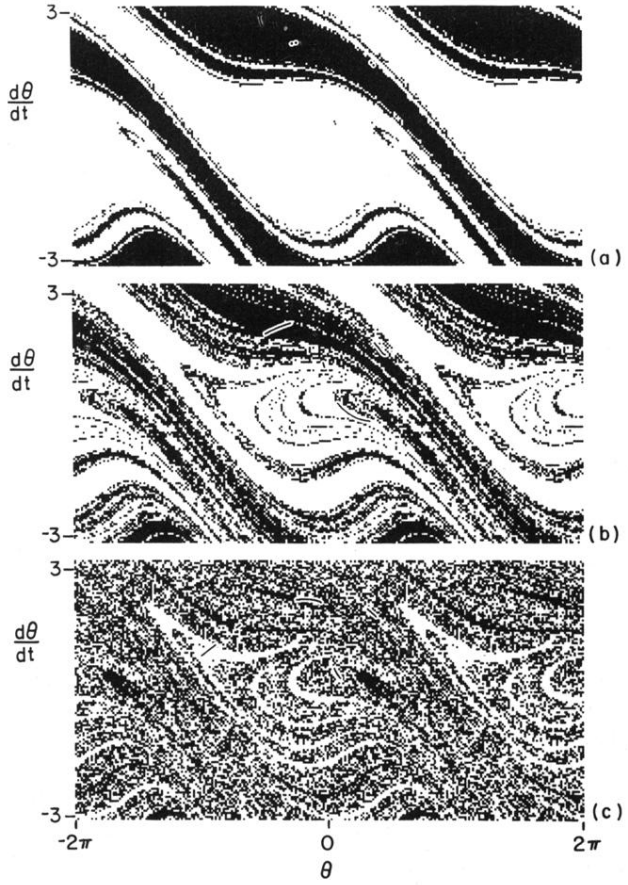

FIG. 3. Basins of attraction for $Q=2$, $\omega_d=\frac{2}{3}$. Basins for attractors with positive average angular velocity are shown as black, and for negative average angular velocity as white. Attractors are plotted from $-\pi$ to π. (a) $g=1.46$. Attractors are periodic. Calculated dimension of basin boundary is 1.63. (b) $g=1.48$. Attractors are chaotic. Calculated dimension of basin boundary is 1.88. (c) $g=1.4954$. Attractors are chaotic. Calculated dimension of basin boundary is 1.97.

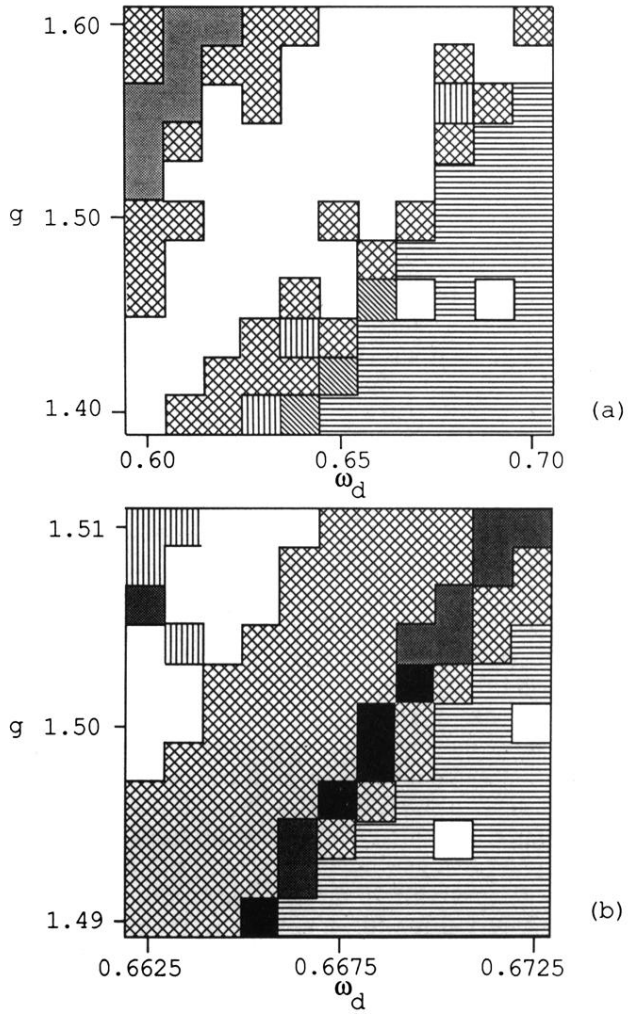

FIG. 4. Phase diagrams centered on $\omega_d = 2/3$ and g_c for $Q = 2$. In both (a) and (b), the final state of the initial condition (0,0,0) is indicated by cross-hatching for intermittency, vertical stripes for nonintermittent chaos with $\langle d\theta/dt \rangle = 0$, white for periodic attractors with $\langle d\theta/dt \rangle = 0$, and horizontal stripes for periodic states with $\langle d\theta/dt \rangle = \pm\omega_d$. (a) $0.60 < \omega_d < 0.70$, $1.40 < g < 1.60$. Shading denotes periodic attractors with $\langle d\theta/dt \rangle = \pm\frac{1}{2}\omega_d$, and diagonal stripes indicate chaotic attractors with $\langle d\theta/dt \rangle = \pm\omega_d$. (b) $0.6625 < \omega_d < 0.6725$, $1.49 < g < 1.51$. Black denotes periodic attractors with $\langle d\theta/dt \rangle = \pm\frac{2}{3}\omega_d$, and gray indicates chaotic attractors with $\langle d\theta/dt \rangle = \pm\frac{2}{3}\omega_d$.

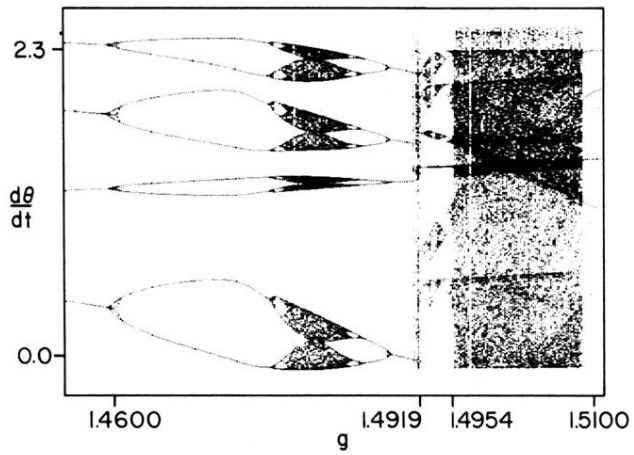

FIG. 6. Bifurcation diagram. The angular velocity is plotted vs g at $\phi=0$ for $\omega_d=\frac{2}{3}$ and $Q=2$.